J. Fluid Mech. (2023), *vol*. 967, A27, doi:10.1017/jfm.2023.500

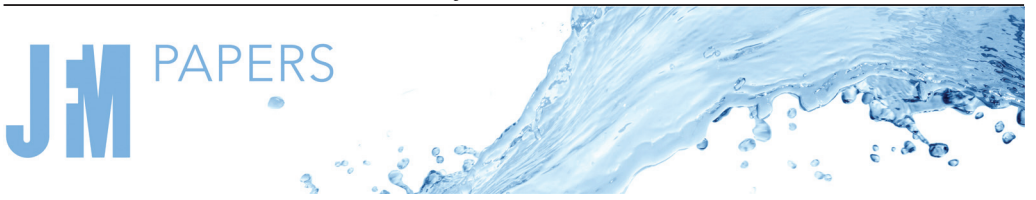

Characteristics of fluid–fluid displacement in model mixed-wet porous media: patterns, pressures and scalings

Ashkan Irannezhad[1], Bauyrzhan K. Primkulov[2], Ruben Juanes[3] and Benzhong Zhao[1,†]

[1]Department of Civil Engineering, McMaster University, Hamilton, Ontario, L8S 4L7, Canada

[2]Department of Mathematics, Massachusetts Institute of Technology, Cambridge, MA 02139, USA

[3]Department of Civil and Environmental Engineering, Massachusetts Institute of Technology, Cambridge, MA 02139, USA

(Received 4 February 2023; revised 8 June 2023; accepted 14 June 2023)

We study numerically the characteristics of fluid–fluid displacement in simple mixed-wet porous micromodels using a dynamic pore network model. The porous micromodel consists of distinct water-wet and oil-wet regions, whose fractions are varied systematically to yield a variety of displacement patterns over a wide range of capillary numbers. We find that the impact of mixed-wettability is most prominent at low capillary numbers, and it depends on the complex interplay between wettability fraction and the intrinsic contact angle of the water-wet regions. For example, the fractal dimension of the displacement pattern is a monotonically increasing function of wettability fraction in flow cells with strongly water-wet clusters, but it becomes non-monotonic with respect to wettability fraction in flow cells with weakly water-wet clusters. Additionally, mixed-wettability also manifests itself in the injection pressure signature, which exhibits fluctuations especially at low wettability fraction. Specifically, preferential filling of water-wet regions leads to reduced effective permeability and higher injection pressure, even at vanishingly small capillary numbers. Finally, we demonstrate that scaling analyses based on a weighted average description of the overall wetting state of the mixed-wet system can effectively capture the variations in observed displacement pattern morphology.

Key words: fingering instability, porous media, capillary flows

† Email address for correspondence: robinzhao@mcmaster.ca

1. Introduction

Fluid–fluid displacement in porous media is a complex phenomenon with significant practical importance. The behaviour of fluid–fluid displacement in porous media impacts various natural and industrial processes such as geological carbon sequestration (MacMinn, Szulczewski & Juanes 2010; Szulczewski *et al.* 2012), water infiltration into soil (Glass, Parlange & Steenhuis 1989; Cueto-Felgueroso & Juanes 2008), enhanced oil recovery (Orr & Taber 1984; Lake 1989), and polymer electrolyte membrane electrolyzers (Lee *et al.* 2019; Zhao *et al.* 2021). Decades of research have illustrated that the displacement process is governed by the competition between capillary and viscous forces as characterized by the capillary number Ca, and the viscosity contrast between the invading and defending fluid as characterized by the viscosity ratio $\mathcal{M}$ (Lenormand, Touboul & Zarcone 1988). In addition, the invading fluid's relative affinity to the solid surface in the presence of the defending fluid (i.e. wettability) as characterized by the contact angle θ also exerts fundamental control over the flow behaviour (Stokes *et al.* 1986; Cieplak & Robbins 1988; Zhao, MacMinn & Juanes 2016). For instance, when the displacing fluid is more wetting to the porous media than the displaced fluid (i.e. imbibition), the fluid–fluid displacement pattern is generally more compact than the opposite case (i.e. drainage) (Holtzman & Segre 2015; Zhao *et al.* 2016; Primkulov *et al.* 2018; Lan *et al.* 2020; Yang *et al.* 2022). Today, we have a fairly good understanding of how the interplay between Ca, $\mathcal{M}$ and θ impacts fluid–fluid displacement in porous media with spatially uniform wettability (Primkulov *et al.* 2021).

In contrast, our knowledge of fluid–fluid displacement in porous media with spatially heterogeneous wettability (i.e. mixed-wet) is much less complete, despite its common occurrence in natural systems. Mixed-wettability in natural porous systems could originate from the spatial variation in mineral composition and surface roughness. Although reservoirs and aquifers consist primarily of water-wet minerals such as quartz and calcite, they also include other constituent minerals with different wettability states (Ustohal, Stauffer & Dracos 1998; Abdallah *et al.* 1986). Moreover, water-wet minerals are known to become oil-wet after exposure to polar hydrocarbon components (e.g. asphaltenes) and some micro-organisms (Tweheyo, Holt & Torsæter 1999; O'Carroll *et al.* 2005; Bultreys, Van Hoorebeke & Cnudde 2016). Indeed, high-resolution *in situ* contact angle measurements of oil-bearing reservoir rocks have shown mixed-wettability with a wide range of contact angles (Andrew, Bijeljic & Blunt 2014; AlRatrout, Blunt & Bijeljic 2018; Blunt *et al.* 2019). In the context of geological carbon sequestration, recent experiments have demonstrated that cyclic injection of supercritical CO_2 and brine altered the wettability of a Bentheimer sandstone core, making it less water-wet (Herring *et al.* 2023).

The behaviour of fluid–fluid displacement in mixed-wet porous media is markedly different from uniform-wet porous media. The significant influence of mixed-wettability on multiphase flow in porous media first emerged in the oil industry, where mixed-wet cores often displayed higher oil displacement efficiency than water-wet cores after waterflooding experiments (Salathiel 1973; Kovscek, Wong & Radke 1993). This behaviour is attributed to the existence of interfaces with very low mean curvature and negative Gaussian curvature (i.e. coexisting curvatures with opposite signs in orthogonal directions; (Lin *et al.* 2019)). Low mean curvature leads to low capillary pressures, while negative Gaussian curvature leads to good connectivity within fluids of the same phase, such that water and oil can flow simultaneously (AlRatrout *et al.* 2018; Lin *et al.* 2019; Scanziani *et al.* 2020). In the context of CO_2 storage, it has been observed that CO_2-brine displacement in mixed-wet rocks results in less CO_2 trapping compared to the same

process in water-wet rocks (Al-Menhali *et al.* 2016; Al-Menhali & Krevor 2016; Chang *et al.* 2020).

Characterizing the wetting state of porous media with heterogeneous wettability is the first step to understanding fluid–fluid displacement in mixed-wet porous media (Armstrong *et al.* 2021). While the wettability of uniform-wet porous media can be described by its contact angle θ, describing the wettability of even the simplest mixed-wet porous media consisting of solids exhibiting just two contact angles requires knowledge of (i) the value of each contact angle, (ii) the fraction of the porous media covered by solids of each contact angle (i.e. wettability fraction), and (iii) the spatial distribution of the wettability heterogeneity as characterized by the correlation length of clusters with different contact angles, as well as their sizes (Guo *et al.* 2020).

Due to the various complexities involved in fully characterizing the wetting state of natural mixed-wet porous media, systematic and mechanistic investigation of the impact of mixed-wettability on fluid–fluid displacement in porous media can be aided greatly by the use of simple analogue systems with well-controlled geometry and wettability states (Murison *et al.* 2014; Hiller *et al.* 2019; Geistlinger *et al.* 2021; Irannezhad *et al.* 2023). Geistlinger *et al.* (2021) performed waterflooding experiments in an air-filled mixed-wet micromodel, which was fabricated by mixing water-wet ($\theta = 0^\circ$) and oil-wet ($\theta = 100^\circ$) glass beads in a cylindrical container. They observed a decrease in residual trapping as the fraction of water-wet beads increased from 30 % to 70 %. Murison *et al.* (2014) conducted waterflooding experiments in oil-filled bead columns where half of the beads' area was water-wet ($\theta = 20^\circ$) while the other half was oil-wet ($\theta = 130^\circ$). They observed smoothing of the fluid–fluid displacement front as the correlation length of different wettability clusters decreased. More recently, Irannezhad *et al.* (2023) studied the radial displacement of oil by water in mixed-wet microfluidic flow cells patterned with cylindrical posts. The bulk of the flow cell was oil-wet ($\theta = 120^\circ$), and mixed-wettability was introduced by placing discrete water-wet clusters that were either weakly water-wet ($\theta = 60^\circ$) or strongly water-wet ($\theta = 30^\circ$). The experiments revealed surprising displacement patterns that arise as a result of mixed-wettability – the invading water preferentially fills strongly water-wet clusters but encircles weakly water-wet clusters instead. This counter-intuitive finding was attributed to the fluid–fluid interface configuration at mixed-wet pores, which resembles S-shaped saddles with mean curvatures close to zero.

While well-designed analogue experiments have contributed to our mechanistic understanding of fluid–fluid displacement in mixed-wet porous media, they remain prohibitively expensive to sweep a wide range of the relevant parameter spaces. Pore-scale modelling is a useful alternative in this endeavour, since it has become increasingly more predictive in recent years (Zhao *et al.* 2016). Bakhshian & Hosseini (2019) investigated the effect of wettability heterogeneity on the flow of supercritical CO_2 and brine in a 1.2 mm^3 digital rock sample using lattice Boltzmann simulations. Specifically, they increased the fraction of CO_2-wet portions of the simulation domain from 10 % to 50 % and observed more residual trapping of CO_2. However, lattice Boltzmann simulations remain computationally challenging and expensive (Zhao *et al.* 2019). In contrast, pore-network models are attractive due to their intuitive nature and relatively low computational cost (Blunt 2001), and they have been applied in a recent study to extend the classic Lenormand's diagram to include the impact of wettability (Primkulov *et al.* 2021).

Here, we employ a dynamic pore network model to investigate the impact of mixed-wettability on fluid–fluid displacement in simple model porous media consisting of water-wet and oil-wet regions with distinct contact angles. For each contact angle pair, we

systematically vary the wettability fraction and study the displacement pattern over a wide range of *Ca*. We find that the displacement pattern is controlled by the interplay between *Ca*, wettability fraction and intrinsic wettability of the water-wet regions, leading to complex behaviours. Furthermore, mixed-wettability induces fluctuations in the injection pressure, whose magnitude has a large viscous component, even at vanishingly small *Ca*. Finally, we demonstrate that scaling analyses based on a simple weighted average description of the overall wettability of the model mixed-wet porous media can effectively predict the finger width of the displacement pattern.

2. Method

We design a microfluidic porous medium by placing ∼16 000 cylindrical posts on an irregular triangular lattice. The lattice is generated inside a 5 inch diameter circle using the pdemesh tool in MATLAB. We assign the radius of each post to be 47 % of the distance between its centre and the nearest neighbouring post's centre. In our system, the radius of the posts follow a Gaussian-like distribution that ranges from 110 to 850 μm, with median value 340 μm. The pore throat sizes follow a lognormal-like distribution that ranges from 50 to 700 μm, with median value 200 μm (Appendix A). We make the posts' height $h = 200$ μm to match the median pore throat size.

We implement mixed-wettability by placing water-wet clusters in a simulation domain that is otherwise oil-wet. Specifically, we randomly assign N posts as the seeds for generating the water-wet clusters. At each seed post, we draw a circle with a radius of five median posts, and make all posts and surfaces within the circle water-wet. Overlapping circles merge and form a single cluster (figure 1*a*). Increasing N increases the wettability fraction f_w, which is defined as the number of water-wet posts out of the total number of posts. In this model, oil-wet and water-wet regions are separated by sharp boundaries connecting the adjacent pore centres (figure 1*a*, top inset). The top and bottom surfaces of the mixed-wet pores also have spatially heterogeneous wettability (figure 1*a*, bottom inset).

We apply a dynamic pore-network model to simulate fluid–fluid displacement in mixed-wet microfluidic cells. The model was first introduced in Irannezhad *et al.* (2023), but we describe its details for the first time here. Our mixed-wet model is based on the model of fluid–fluid displacement in uniform-wet porous media developed by Primkulov *et al.* (2019). The model establishes an analogy between multiphase flow in porous media and electrical current in a circuit with fixed resistors and moving capacitors. This analogy enables the model to capture the effects of capillary pressure (at pore throats where fluid–fluid interfaces exist) and viscous pressure drop (at all pore throats) simultaneously throughout the network. Adding wettability effects to the model requires an understanding of invasion mechanisms at the pore scale, where fluid–fluid interfaces advance as invading fluid pressure increases. This advancement leads eventually to the invasion of the adjacent pore through one of the three possible types of invasion events (Cieplak & Robbins 1988, 1990), as follows. (i) Burst is equivalent to a Haines jump (Haines 1930), and occurs when there is no stable configuration for a fluid–fluid interface connecting two posts. Thus the interface suddenly invades the adjacent pore and splits into two interfaces. (ii) Touch occurs when the fluid–fluid interface connecting two posts touches a third post's body. Similar to the burst event, the fluid–fluid interface splits into two interfaces. (iii) Overlap occurs when two neighbouring fluid–fluid interfaces meet on a common post. In this case, the two interfaces merge and form a single, wider interface spanning the

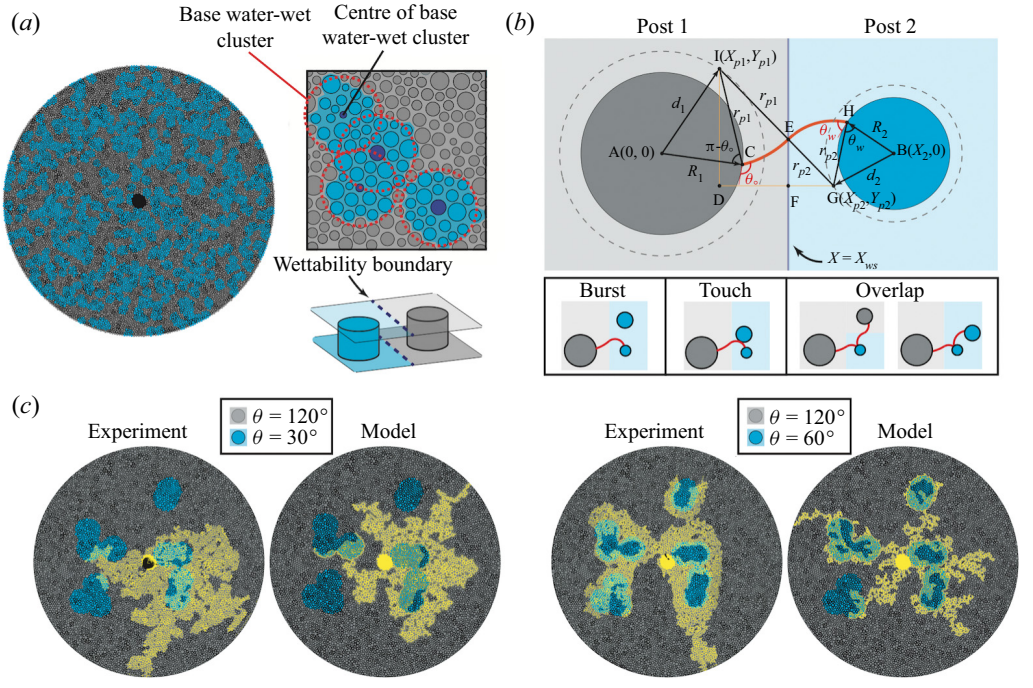

Figure 1. (*a*) We develop a dynamic pore network model to simulate fluid–fluid displacement through analogue porous media with spatially heterogeneous wettability (i.e. mixed-wet). The flow geometry is radial and quasi-two-dimensional, consisting of ∼16 000 cylindrical posts. We achieve mixed-wettability by placing base water-wet clusters (blue regions) that span five posts in a domain that is otherwise oil-wet (grey regions). The base water-wet clusters merge and form larger clusters (top inset). The water-wet and oil-wet regions are separated by sharp boundaries (bottom inset). (*b*) The fluid–fluid interface at a mixed-wet pore throat resembles an S-shaped saddle in three dimensions (Irannezhad *et al.* 2023). Our model calculates explicitly the critical pressures of pore-scale instabilities and advances the fluid–fluid interface when a burst, touch or overlap event occurs. (*c*) Our pore network model captures the nuanced and complex behaviour of multiphase flow in mixed-wet porous media (Irannezhad *et al.* 2023). The invading water (yellow) preferentially fills the water-wet clusters with contact angle $\theta = 30^\circ$ (left-hand plots), but encircles the water-wet clusters with $\theta = 60^\circ$ (right-hand plots). The oil-wet clusters have $\theta = 120^\circ$ in both cases. Experiments and simulations are conducted at $Ca = 1 \times 10^{-4}$ (Irannezhad *et al.* 2023).

neighbouring posts. The configuration of any given fluid–fluid interface can be described by its in-plane and out-of-plane curvatures.

In a quasi-two-dimensional, uniform-wet microfluidic cell, the interface's out-of-plane radius of curvature r_{out} is constant and equal to $h/(2\cos\theta)$, while its in-plane radius of curvature r_{in} decreases as the interface advances through the pore throat. Therefore, capillary pressure at the interface gradually increases as the interface advances, until the interface undergoes an invasion event (i.e. burst, touch or overlap). The capillary pressure associated with pore invasion is termed the critical capillary pressure, and is given by $p_c^{crit} = \sigma/r_{out} + \min(\sigma/r_{in}^{burst}, \sigma/r_{in}^{touch}, \sigma/r_{in}^{overlap})$, where σ is the interfacial tension between the two fluids, and r_{in}^{burst}, r_{in}^{touch}, $r_{in}^{overlap}$ are the in-plane radii of curvature corresponding to burst, touch and overlap events, respectively. These in-plane radii of curvature for pore invasion mechanisms in a uniform-wet microfluidic cell have been derived in Primkulov *et al.* (2018).

The fluid–fluid interface configuration at a mixed-wet pore throat is more complex. In particular, the interface has been observed to be saddle-shaped (Lin *et al.* 2019). Additionally, *in situ* measurements of fluid–fluid interfaces in carbonate rocks have revealed that their mean curvatures are noticeably lower in mixed-wet rocks compared to similar water-wet rocks (Armstrong & Wildenschild 2012; Lin *et al.* 2019). Recent experiments in mixed-wet microfluidics provided high-resolution visualization of the fluid–fluid interface between two posts of contrasting wettabilities, which resembles an S-shaped saddle in three dimensions, with mean curvatures close to zero (Irannezhad *et al.* 2023).

The in-plane view of a typical S-shaped fluid–fluid interface at a mixed-wet pore throat is shown in figure 1(*b*). Post 1 is an oil-wet post with contact angle θ_o, radius R_1, and centre coordinate A$(0, 0)$, while post 2 is a water-wet post with contact angle θ_w, radius R_2, and centre coordinate B$(X_2, 0)$. We approximate the S-shaped interface as two circular arcs ($\overset{\frown}{CE}$ and $\overset{\frown}{EH}$) that connect smoothly at the wettability boundary. The centres of $\overset{\frown}{CE}$ and $\overset{\frown}{EH}$ are located at I(X_{p1}, Y_{p1}) and G(X_{p2}, Y_{p2}), while their radii are given by r_{p1} and r_{p2}, respectively. We denote the distance between points A and I as d_1, which is given by the cosine law in the triangle AIC as

$$d_1 = \sqrt{R_1^2 + r_{p1}^2 - 2R_1 r_{p1}\cos(\pi - \theta_o)}. \tag{2.1}$$

Similarly, the distance d_2 between points B and H is given by

$$d_2 = \sqrt{R_2^2 + r_{p2}^2 - 2R_2 r_{p2}\cos\theta_w}. \tag{2.2}$$

As the fluid–fluid interface advances through the pore throat, point I and point G each trace a circle described by

$$X_{p1}^2 + Y_{p1}^2 = d_1^2, \tag{2.3a}$$

$$(X_{p2} - X_2)^2 + Y_{p2}^2 = d_2^2. \tag{2.3b}$$

Since $\overset{\frown}{CE}$ and $\overset{\frown}{EH}$ join smoothly at point E, we construct the right triangle IGD and find the distance d_3 between points I and G:

$$d_3 = r_{p1} + r_{p2} = \sqrt{(X_{p2} - X_{p1})^2 + (Y_{p1} - Y_{p2})^2}. \tag{2.4}$$

Furthermore, the right triangles IGD and EGF are similar triangles, which leads to

$$\frac{r_{p2}}{r_{p1} + r_{p2}} = \frac{X_{p2} - X_{wb}}{X_{p2} - X_{p1}}, \tag{2.5}$$

where X_{wb} is the x-coordinate of the wettability boundary.

Finally, we note that the mean curvature of the fluid–fluid interface in the oil-wet region must equal that in the water-wet region at equilibrium, since capillary pressure is constant along the entire interface. Therefore,

$$\frac{1}{r_{p1}} + \frac{2\cos\theta_o}{h} = -\frac{1}{r_{p2}} + \frac{2\cos\theta_w}{h}. \tag{2.6}$$

The shape of the fluid–fluid interface at the mixed-wet pore throat is described fully by X_{p1}, Y_{p1}, X_{p2}, Y_{p2}, r_{p1} and r_{p2}. For a given r_{p1}, we first solve for r_{p2} in (2.6). We then solve for d_1 and d_2 in (2.1)–(2.2), followed by solving for X_{p1}, Y_{p1}, X_{p2} and Y_{p2} in (2.3)–(2.5).

We follow the algorithm below to find the critical capillary pressures associated with burst, touch and overlap invasion events. Starting with a large r_{p1}, we solve (2.1)–(2.6). If no valid solution is found, then we decrease r_{p1} and repeat the process until a valid fluid–fluid interface is found. We then depict the interface and check if touch or overlap will occur. Touch occurs when the depicted interface intersects a neighbouring third post, while overlap occurs when the depicted interface intersects an adjacent interface (Cieplak & Robbins 1988, 1990). We decrease r_{p1} successively until no valid solution can be found, which corresponds to the point when burst occurs. Similar to the homogeneous-wet case, the critical capillary pressure for pore invasion is given by

$$p_c^{crit} = \frac{2\sigma\cos\theta_o}{h} + \min(\sigma/r_{p1}^{burst}, \sigma/r_{p1}^{touch}, \sigma/r_{p1}^{overlap}). \tag{2.7}$$

Our model captures the effects of viscous pressure drop across the system by solving the equations of Poiseuille's law and mass conservation for the network of pore throats. We impose a constant flow boundary condition at the inlet pore throats, and a constant pressure boundary condition at the outlet pores along the perimeter. We assign the viscosities of the defending fluid and the invading fluid to be $\mu_{def} = 50$ mPa s and $\mu_{\text{inv}} = 0.99$ mPa s, respectively, and the interfacial tension between the fluids to be $\sigma = 13$ mN m^{-1}. These fluid–fluid properties correspond to the microfluidic experiments of Irannezhad *et al.* (2023), which enables direct comparison between the model predictions and the experiments. Specifically, the model captures the salient behaviours of the mixed-wet microfluidic experiment – the invading fluid preferentially fills the water-wet clusters with contact angle $\theta = 30^\circ$, but encircles the weakly water-wet clusters with contact angle $\theta = 60^\circ$ instead (figure 1*c*). The oil-wet regions of the flow cell have contact angle $\theta = 120^\circ$ in both cases.

3. Results

3.1. *Phase diagram*

We apply the dynamic pore-network model to investigate fluid–fluid displacement in simple mixed-wet microfluidics. Specifically, each simulation domain consists of water-wet regions with contact angle θ_w and oil-wet regions with contact angle θ_o. We consider three different contact angle pairs: θ_w–$\theta_o = 30^\circ$–120°, 60°–120° and 60°–150°. Our systematic investigation includes varying the wettability fraction ($f_w = 2\,\%$, $26\,\%$, $50\,\%$, $76\,\%$, $98\,\%$) and capillary number ($Ca = 5\times10^{-4}$, 1×10^{-4}, 5×10^{-5}, 1×10^{-5}, 5×10^{-6}) over a wide range of values. Here, the macroscopic $Ca = \mu_o v/\sigma$ measures the relative importance between viscous and capillary forces. The characteristic velocity is defined as $v = Q/(h2\pi r_{in})$, where r_{in} is the distance between the cell's centre and its closest post. Additionally, for each f_w, we design three mixed-wet cells with different base water-wet cluster placements to verify the reproducibility of the results. Figure 2 shows the phase diagrams of the fluid–fluid displacement patterns in mixed-wet domains consisting of the three contact angle pairs, at different Ca and f_w. Qualitatively, the displacements display the canonical viscous fingering pattern at high Ca for all mixed-wettability conditions. As Ca decreases, the displacement patterns become more compact with increasing f_w, though this effect is much more noticeable in mixed-wet domains with contact angle pair 30°–120° compared to domains with contact angle pairs 60°–120° and 60°–150°.

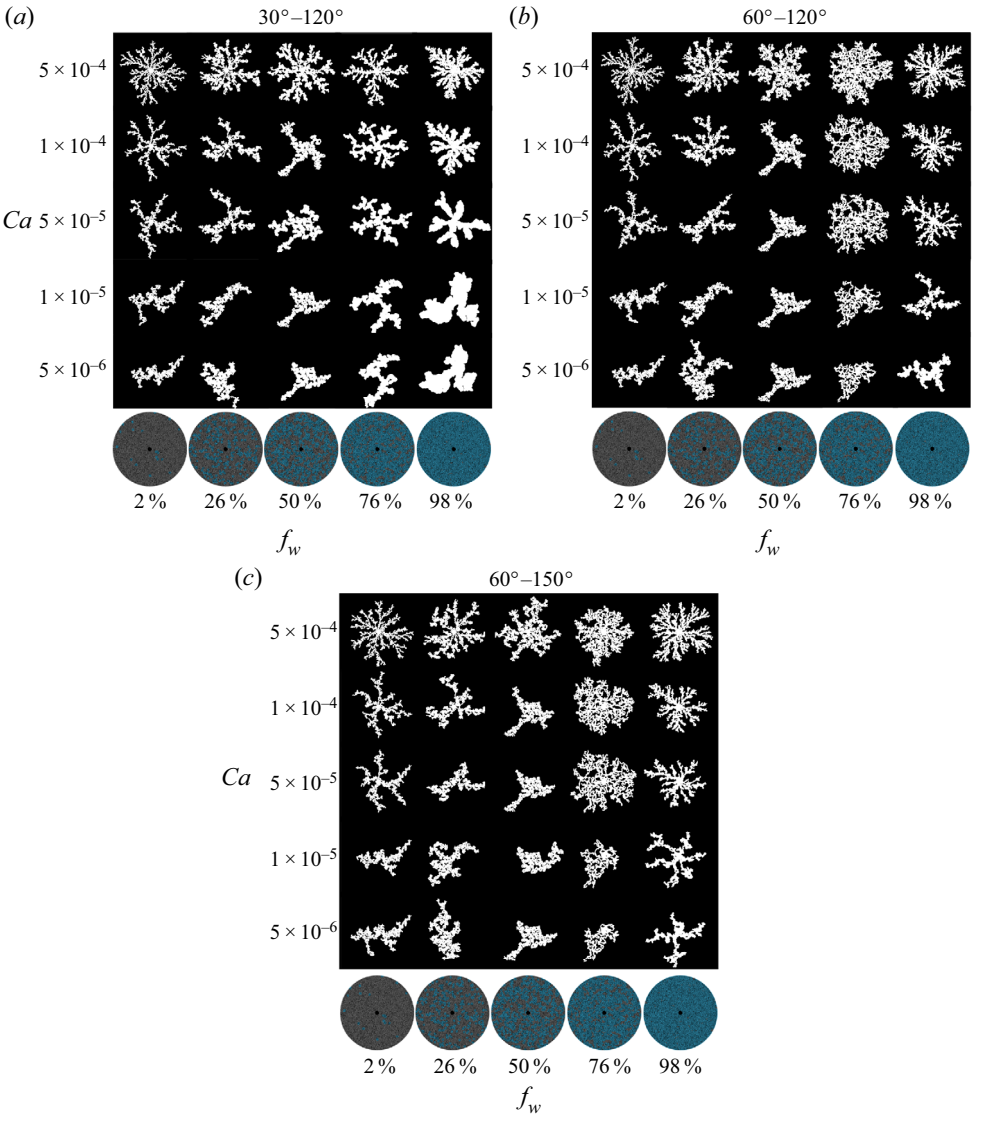

Figure 2. Phase diagrams of the invading fluid morphology at breakthrough for different wettability fractions (left to right 2 %, 26 %, 50 %, 76 %, 98 %) and capillary numbers (top to bottom $Ca = 5 \times 10^{-4}$, 1×10^{-4}, 5×10^{-5}, 1×10^{-5}, 5×10^{-6}). Phase diagrams corresponding to mixed-wet porous media with contact angle pairs (*a*) 30°–120°, (*b*) 60°–120°, and (*c*) 60°–150°.

3.2. *Quantitative measures*

To quantify the morphological properties of the displacement patterns, we calculate the dimensionless finger width (w_f) and the fractal dimension (D_f). Here, D_f is calculated via the box-counting method (Kenkel & Walker 1996; Schroeder 2009), while w_f is defined as the average finger width normalized by the average pore size (Cieplak & Robbins 1988, 1990; Holtzman 2016; Primkulov *et al.* 2019).

Increasing Ca leads to smaller w_f in all mixed-wet domains due to viscous effects. Increasing f_w yields only moderately higher w_f in mixed-wet domains with contact angle

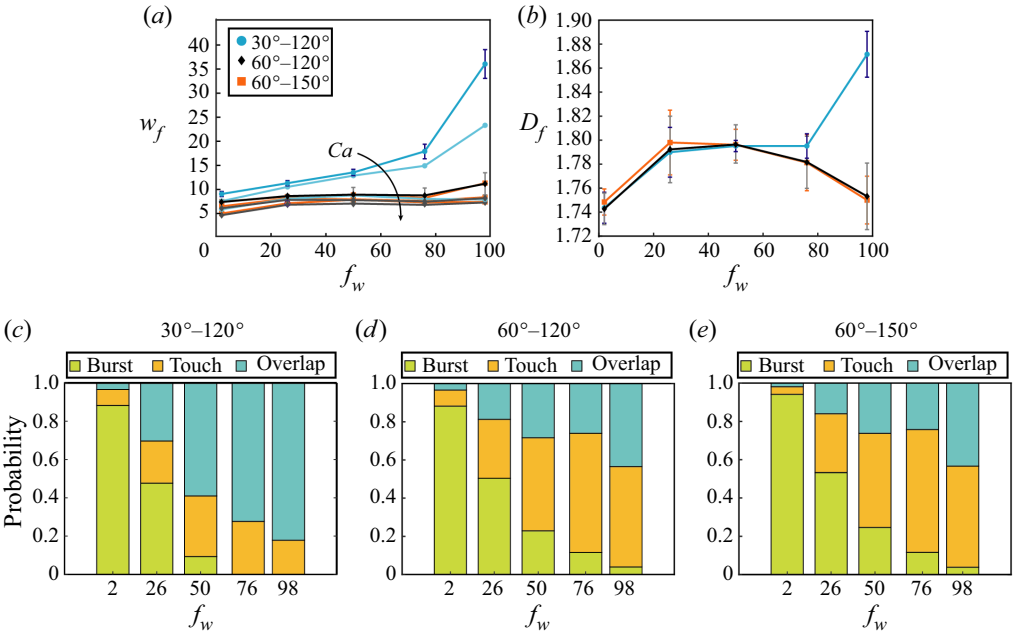

Figure 3. Quantitative measures of the displacement patterns. (*a*) Normalized finger width for three capillary numbers ($Ca = 5 \times 10^{-6}$, 5×10^{-5}, 5×10^{-4}), and (*b*) fractal dimension for the lowest capillary number in mixed-wet domains, with contact angle pairs 30°–120° (blue circles), 60°–120° (black diamonds) and 60°–150° (orange squares). Distributions of burst, touch and overlap events as functions of f_w in mixed-wet domains with contact angle pairs (*c*) 30°–120°, (*d*) 60°–120° and (*e*) 60°–150°, for displacements at the lowest capillary number.

pairs 60°–120° and 60°–150°, though the positive correlation between w_f and f_w is significantly more prominent in mixed-wet domains with contact angle pair 30°–120° (figure 3*a*). Variations in w_f can be explained by the pore-scale invasion mechanism. The dominant pore invasion mechanism in oil-wet porous media is burst, while pores in water-wet porous media experience more overlap (Primkulov *et al.* 2018, 2019). During overlap events, the invasion of one pore destabilizes the fluid–fluid interface at the neighbouring pore, creating a smoother displacement front (Cieplak & Robbins 1988, 1990; Holtzman & Segre 2015). Therefore, w_f increases with increasing f_w. Furthermore, the probability of overlap events occurring increases as the invading fluid becomes more wetting to the porous media (Holtzman & Segre 2015; Primkulov *et al.* 2018, 2019). Indeed, tracking the invasion event type reveals that increase in overlap events with increasing f_w is much more significant in mixed-wet domains with contact angle pair 30°–120°, compared to the mixed-wet domains with contact angle pairs 60°–120° and 60°–150° (figures 3*c–e*).

We measure the fractal dimension of the displacement patterns at the lowest capillary number ($Ca = 5 \times 10^{-6}$), which characterizes the extent to which the displacement patterns fill space in two dimensions (figure 3*b*). As expected, D_f increases with increasing f_w in mixed-wet domains with contact angle pair 30°–120° due to the rise in overlap-driven smoothing of the displacement front. However, this is not the case in mixed-wet domains with contact angle pairs 60°–120° and 60°–150°, where D_f is a non-monotonic function of f_w, and D_f reaches a maximum at $f_w = 50\,\%$. This surprising behaviour can be rationalized by the following arguments. At low f_w, the broadening of the displacement pattern is

controlled by the size and distribution of the water-wet clusters – increasing the size and number of water-wet clusters increases D_f. At high f_w, however, the broadening of the displacement pattern is controlled by the intrinsic wettability of the water-wet clusters – more strongly water-wet clusters will yield higher D_f due to a higher probability of overlap events. We note that such contrasting behaviours have been observed in waterflooding experiments in mixed-wet oil-bearing porous media. For instance, Singhal, Mukherjee & Somerton (1976) found that oil recovery efficiency increases monotonically as the fraction of the water-wet surface area of the porous medium increases. In contrast, Skauge & Ottesen (2002) and Høiland, Spildo & Skauge (2007) found that oil recovery efficiency shows a non-monotonic trend according to wettability, with highly mixed-wet cores showing higher oil recovery efficiency than mostly water-wet and oil-wet cores.

3.3. *Pressure signatures*

We track the injection pressure evolution to gain further insight into the macroscopic impact of mixed-wettability on fluid–fluid displacement in porous media. Injection pressure is a valuable piece of information in various subsurface applications, including geological carbon sequestration (Bachu 2008) and hydraulic fracturing (Warner *et al.* 2012), and it can help to inform the wettability state of the porous medium (Sygouni, Tsakiroglou & Payatakes 2006). The injection pressure consists of the capillary pressure across the interface between the invading and defending fluids, and the combined viscous pressure loss in the two fluids.

At high Ca, viscous pressure loss dominates, and the injection pressure decreases monotonically as the more viscous defending fluid is pushed out by the less viscous invading fluid. This decreasing trend in injection pressure is observed in all cases, regardless of the wettability state of the domain (figure 4*a*). Interestingly, the signature of wettability is evident even at the highest capillary number ($Ca = 5 \times 10^{-4}$) – the injection pressure is consistently higher in a purely oil-wet domain compared to a purely water-wet domain. These results agree with the injection pressure measurements in uniform-wet microfluidic experiments (Zhao *et al.* 2016). The injection pressures observed in mixed-wet domains fall between those in purely oil-wet and water-wet domains (figure 4*a*).

At low Ca, capillary pressure dominates and the injection pressure is controlled by the wettability of the domain. Indeed, the injection pressure fluctuates around a mean positive value in a purely oil-wet domain (i.e. drainage), but around a mean negative value in a purely water-wet domain (i.e. imbibition). Closer inspection shows that the injection pressure fluctuations are larger in a purely oil-wet domain than in a purely water-wet domain (figures 4*b*,*c*). This difference in fluctuations is attributed to the prevalence of burst invasion events in drainage, whose critical capillary pressures are larger than those of touch and overlap invasion events, which are more prevalent in imbibition (Måløy *et al.* 1992; Moebius & Or 2012; Primkulov *et al.* 2019).

Intuitively, at vanishingly small Ca, one would expect the injection pressure to fluctuate between the drainage capillary pressure and the imbibition capillary pressure in a mixed-wet domain, as the invading water transits oil-wet and water-wet clusters. Surprisingly, this is not what we see in mixed-wet domains with small f_w – instead, we observe that the injection pressure fluctuates between the drainage capillary pressure and some pressure that is much higher than the imbibition capillary pressure (figure 4*b*). This deviation can be explained by the fact that once the invading water encounters a water-wet cluster, all of the injected volume will preferentially enter that region of the micromodel. Since the water-wet clusters are small at low f_w, the preferential filling within

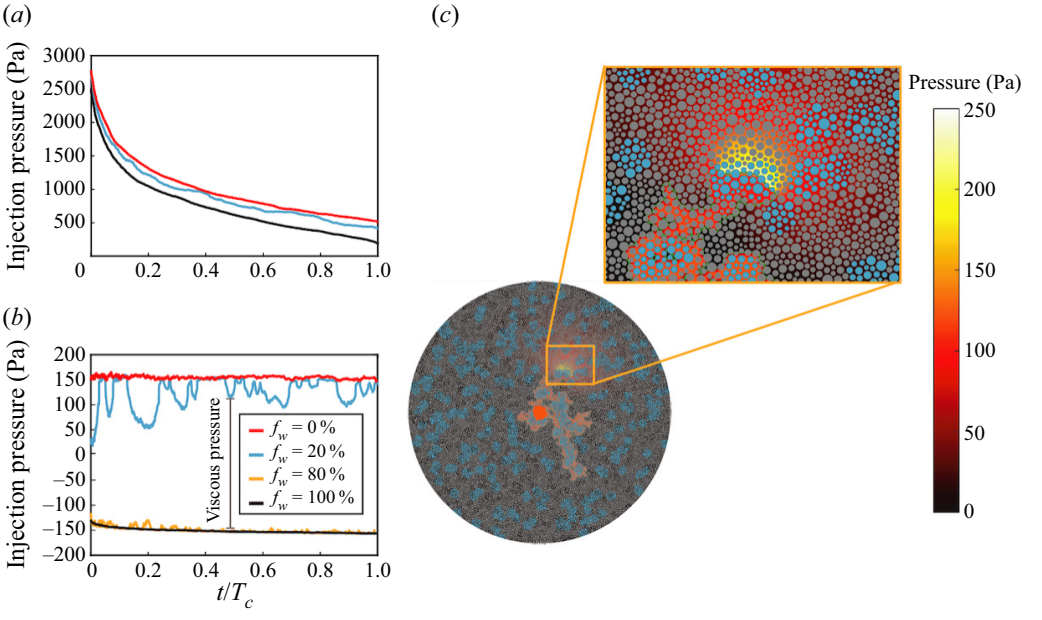

Figure 4. Evolution of injection pressure as a function of f_w at (*a*) a high capillary number ($Ca = 5 \times 10^{-4}$) and (*b*) a low capillary number ($Ca = 5 \times 10^{-6}$), for different wettability fractions. The water-wet region has contact angle $\theta_w = 30^\circ$, while the oil-wet region has contact angle $\theta_o = 120^\circ$. (*c*) Snapshot of the pressure map as the invading water fills a water-wet cluster at $Ca = 5 \times 10^{-6}$ for $f_w = 20\,\%$. The preferential filling of the water-wet cluster causes the local redistribution of the defending oil, leading to non-negligible viscous pressure loss even at very low *Ca*.

this localized region will cause the defending fluid to redistribute along the invasion front, leading to non-negligible viscous pressure loss even at very low *Ca*. Indeed, as the invading water enters a water-wet cluster ($\theta_w = 30^\circ$, $f_w = 20\,\%$), the difference between the measured injection pressure and the imbibition capillary pressure equals the viscous pressure in the defending oil (figure 4*c*). Therefore, mixed-wettability could decrease the effective permeability of porous media at low *Ca*. As the invading water exits the water-wet cluster, the injection pressure increases to the drainage capillary pressure. Consequently, the period of the fluctuations indicates the size of the water-wet cluster. At high f_w, the invading water has access to many connected water-wet pores at any given time, and the injection pressure closely tracks the imbibition capillary pressure (figure 4*b*).

3.4. *Wettability index description of mixed-wet systems*

Despite the complexities involved in fully characterizing the wettability of mixed-wet systems (e.g. contact angles, wettability fraction), it is sometimes helpful to approximate the wettability state of a porous medium by a single parameter. One of the simplest representations of this idea is the wettability index (WI), which in its general form is given by (Armstrong *et al.* 2021)

$$\mathrm{WI} = \sum_{i=1}^{n} \frac{\sigma_{i1} - \sigma_{i2}}{\sigma_{12}} f_i, \tag{3.1}$$

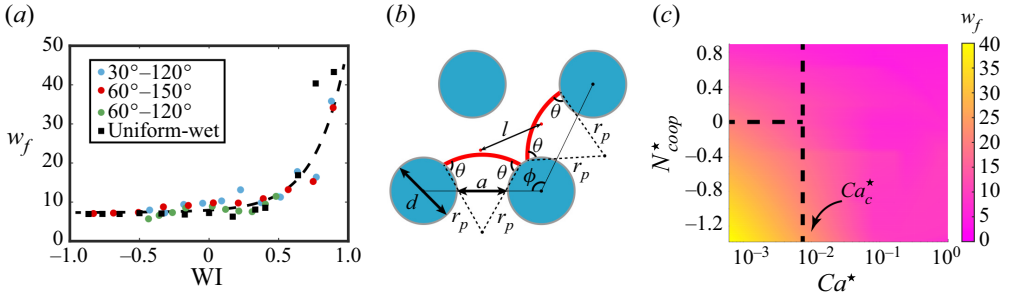

Figure 5. Wettability index description of mixed-wet systems. (*a*) We extract the average finger width w_f from fluid–fluid displacement simulations in more than 50 mixed-wet porous media of different contact angle pairs (θ_w–$\theta_o = 30°$–$120°$, $60°$–$120°$, $60°$–$150°$) and wettability fractions. Plotting w_f versus the wettability index (WI) collapses the dataset onto a single curve, which matches the results obtained from simulations performed in uniform-wet porous media with different wettabilities. In all simulations, $Ca = 5 \times 10^{-6}$. (*b*) Invasion front configuration at two adjacent pores. (*c*) Here, $Ca^\star$ and $N^\star_{coop}$ explain the variations in w_f in 15 different mixed-wet domains (θ_w–$\theta_o = 30°$–$120°$, $60°$–$120°$, $60°$–$150°$; $f_w = 2\,\%, 26\,\%, 50\,\%, 76\,\%, 98\,\%$) over a wide range of capillary numbers.

where f_i is the area fraction of surface i, σ_{12} is the interfacial tension between fluid 1 and fluid 2, and σ_{i1}, σ_{i2} are the interfacial tensions between surface i and the two fluids. Young's equation relates the interfacial tensions to the contact angle. For our mixed-wet system with two distinct contact angles and oil-water as the fluid–fluid pair, incorporating Young's equation gives

$$\mathrm{WI} = f_w \cos\theta_w + (1 - f_w)\cos\theta_o. \tag{3.2}$$

Therefore, WI is a weighted average description of the overall wettability of the porous media. Here, we examine the effectiveness of WI in predicting the fluid–fluid displacement pattern as characterized by the finger width w_f at low capillary number ($Ca = 5 \times 10^{-6}$). We find that WI successfully collapses w_f extracted from simulations conducted in more than 50 different mixed-wet porous media. Additionally, this master curve matches the one obtained from simulations of fluid–fluid displacement in uniform-wet porous media, which both show that finger width increases with increasing WI (figure 5*a*).

We take the weighted average description of fluid–fluid displacement in mixed-wet porous media one step further via scaling analysis and derive two dimensionless parameters that capture the behaviour of w_f across all Ca. We first compare the relative importance of the characteristic viscous pressure δp_v and capillary pressure δp_c at the pore scale (Toussaint *et al.* 2005; Holtzman & Juanes 2010; Holtzman 2016; Primkulov *et al.* 2019). The characteristic viscous pressure is given by the pressure drop in the viscous defending fluid over a characteristic length l:

$$\delta p_v = 32\mu_{def}\, v\, \frac{(a+h)^2}{a^2h^2}\, l, \tag{3.3}$$

where v is the characteristic injection velocity, and a and l are the median pore length and pore throat size, respectively. The characteristic capillary pressure is assumed to be the

capillary pressure corresponding to a burst event at a characteristic pore throat:

$$\delta p_c = \sigma\kappa, \tag{3.4a}$$

$$\kappa = \frac{2\cos\theta}{h} + \frac{2}{a\left(\hat{l}\cos\theta + \sqrt{\hat{l}^2(\cos\theta)^2 + 1 + 2\hat{l}}\right)}, \tag{3.4b}$$

where κ is the critical interface curvature required for burst to occur, and $\hat{l} = d/a$ is the ratio between the median post diameter and the median pore throat size (figure 5*b*). (A detailed derivation of (3.4*b*) is included in Appendix B.) The ratio between δp_v and δp_c yields a modified capillary number $Ca^\star$, which takes into account the wettability of the system (Holtzman & Segre 2015; Holtzman 2016; Primkulov *et al.* 2019). In our mixed-wet system, water-wet and oil-wet regions have the same characteristic viscous pressure drop, but noticeably different capillary pressure. We take the weighted average of the characteristic capillary pressures in the water-wet and oil-wet regions, and arrive at

$$Ca^\star = \frac{32(a+h)^2 l}{a^2h^2(f_w\kappa_w + (1-f_w)\kappa_o)}\,Ca, \tag{3.5}$$

where κ_w and κ_o are the critical interface curvatures (3.4*b*) for water-wet and oil-wet regions, respectively.

On its own, $Ca^\star$ is not able to capture the displacement pattern across different wettabilities, since it does not account for the different types of invasion events (i.e. burst, touch, overlap). It is well-known that overlap events promote cooperative pore filling, which leads to more compact displacement (i.e. wider fingers; Cieplak & Robbins 1988, 1990; Zhao *et al.* 2016; Primkulov *et al.* 2018). To capture the effect of cooperative pore filling, we calculate the dimensionless cooperative number (N_{coop}) for our system. Specifically, N_{coop} evaluates the relative likelihood of overlap and burst events by comparing the critical capillary pressures associated with the two invasion event types (Holtzman & Segre 2015). For a characteristic pore, N_{coop} is given by

$$N_{coop} = \frac{\phi}{2} + \theta + \arccos\left(\frac{r_p^2 + d_1^2 - \dfrac{d^2}{4}}{2d_1 r_p}\right) + \arccos\left(\frac{a+d}{2d_1}\right) - \pi, \tag{3.6a}$$

$$r_p = \frac{\hat{l}\cos\theta + \sqrt{\hat{l}^2(\cos\theta)^2 + 1 + 2\hat{l}}}{\dfrac{2}{a}}, \tag{3.6b}$$

where ϕ is the median angle between two neighbouring interfaces. (A detailed derivation of N_{coop} is included in Appendix C.) Positive N_{coop} indicates that burst events are more likely to occur than overlap, while negative N_{coop} suggests the opposite. Finally, we take the weighted average of the cooperative numbers for the water-wet region ($N_{coop,w}$) and the oil-wet region ($N_{coop,o}$) to arrive at a modified cooperative number for the mixed-wet system:

$$N^\star_{coop} = f_w N_{coop,w} + (1-f_w)N_{coop,o}. \tag{3.7}$$

Here, $Ca^\star$ and $N^\star_{coop}$ explain the variations in w_f in different mixed-wet domains over a wide range of capillary numbers (figure 5*c*, figure 9). In our system, the critical modified

capillary number is $Ca_c^\star \sim d/D \approx 6 \times 10^{-3}$, where D is the diameter of the domain. For $Ca^\star > Ca_c^\star$, viscous pressure dominates, and the displacement pattern consists of long, thin fingers (small w_f) that are typical in viscous fingering. For $Ca^\star < Ca_c^\star$, the displacement pattern is dependent upon the amount of cooperative smoothing in the system such that wide fingers (large w_f) start to emerge for $N_{coop}^\star < 0$.

4. Conclusions

We have investigated fluid–fluid displacement in simple mixed-wet porous media consisting of distinct water-wet and oil-wet regions using a dynamic pore network model. We generate phase diagrams of the displacement patterns for three different water-wet/oil-wet contact angle pairs over a wide range of Ca (figure 2). The impact of mixed-wettability is most prominent at low Ca, whose effect on the displacement pattern is controlled by the complex interplay between wettability fraction and the intrinsic contact angle of the water-wet regions (figure 3). Our simulations also provide insights into the pressure signature of fluid–fluid displacement in mixed-wet porous media, which displays fluctuations that cannot be explained by capillary pressure alone, even at vanishingly small Ca (figure 4). We find that the injection pressure fluctuations are modulated by the viscous pressure of the defending fluid due to preferential filling of isolated water-wet regions, and the durations of the fluctuations are determined by the sizes of the water-wet regions. One surprising consequence of this complex interplay is that at low Ca, mixed-wettability could result simultaneously in reduced effective permeability, but more effective sweep of the defending fluid. Finally, we derive scaling arguments based on a weighted average description of the overall wettability of the mixed-wet porous medium, which effectively capture the variations in displacement pattern morphology as characterized by the finger width (figure 5). Our study presents a systematic understanding of the relationship between contact angle, wettability fraction and capillary number in governing fluid–fluid displacement in simple mixed-wet porous media, and it serves as a platform upon which more complex mixed-wet porous media can be investigated. For instance, the impact of spatial distribution of wettability clusters, including mixed-wettability at the scale of a single pore, as well as the interaction between pore size disorder and wettability heterogeneity, remain as interesting areas for further study.

Funding. This research was supported by the Natural Sciences and Engineering Research Council of Canada (NSERC) Discovery Grants (RGPIN-2019-07162).

Declaration of interests. The authors report no conflict of interest.

Author ORCIDs.
Bauyrzhan K. Primkulov https://orcid.org/0000-0002-8162-2471;
Ruben Juanes https://orcid.org/0000-0002-7370-2332;
Benzhong Zhao https://orcid.org/0000-0003-1136-9957.

Appendix A. Model geometry

In our system, the diameters of the posts follow a Gaussian-like distribution that ranges from 220 to 1700 μm (figure 6*a*). Additionally, the pore throat size follows a lognormal-like distribution that ranges from 50 to 700 μm (figure 6*b*).

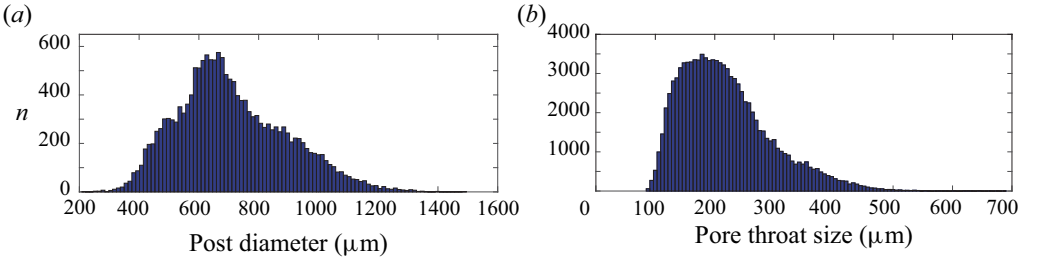

Figure 6. Characteristics of the micromodel domain: (*a*) post diameter; (*b*) pore throat size.

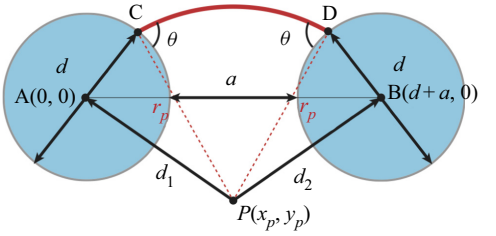

Figure 7. Fluid–fluid interface configuration at a median-size pore throat.

Appendix B. Critical interface curvature for burst

Our aim here is to determine the critical interface curvature for a burst to occur in a typical pore throat configuration in the model. In this configuration, the fluid–fluid interface connects two posts with diameters d (i.e. the median post diameter in the system), where the closest distance between these posts is equal to a (i.e. the median pore throat size in the system). The wettability of the posts is the same, and their contact angles are equal to θ. After translation and rotation of the coordinate system, the centre of post A is positioned at $(0, 0)$, and the centre of post B is located at $(a + d, 0)$. Figure 7 shows the fluid–fluid interface arc $\overset{\frown}{CD}$ with the centre $\mathrm{P}(x_p, y_p)$ in the pore throat. We denote the distance between points A and P as d_1, which is given by the cosine law at the triangle APC as

$$d_1 = \sqrt{\left(\frac{d}{2}\right)^2 + r_p^2 - 2\left(\frac{d}{2}\right) r_p \cos\theta}. \tag{B1}$$

We denote the distance between points B and P as d_2, which is equal to d_1.

As defined in Primkulov *et al.* (2018), a burst event occurs when the centre of the fluid–fluid interface has the configuration

$$X_p^2 = d_1^2, \tag{B2}$$

$$(X_p - X_2)^2 = d_2^2, \tag{B3}$$

where X_2 is the x coordinate of the centre of post B, and it is equal to $a + d$. Solving (B1)–(B3), we find the radius of curvature of the fluid–fluid interface corresponding to a

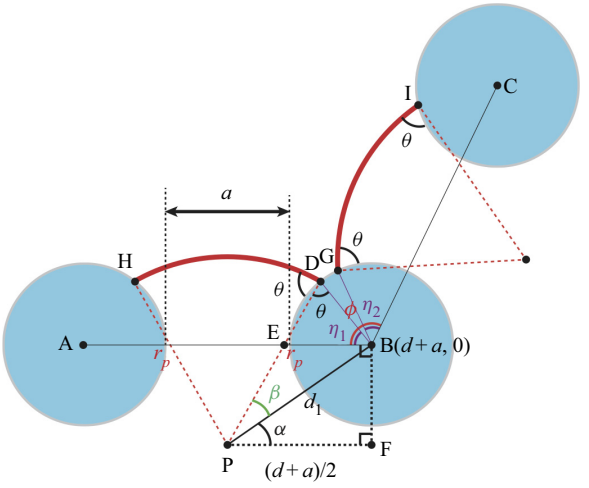

Figure 8. Fluid–fluid interface configurations at two neighbouring pore throats.

burst event as

$$r_p = \frac{\hat{l}\cos\theta + \sqrt{\hat{l}^2(\cos\theta)^2 + 1 + 2\hat{l}}}{\frac{2}{a}}, \tag{B4}$$

where $\hat{l} = d/a$. The mean curvature of the interface at a burst event is defined as $\kappa = (1/r_p + 1/r_{out})$, where $r_{out} = h/(2\cos\theta)$ is the out-of-plane curvature of the interface. Consequently, the critical interface curvature for a burst to occur is equal to

$$\kappa = \frac{2\cos\theta}{h} + \frac{2}{a\left(\hat{l}\cos\theta + \sqrt{\hat{l}^2(\cos\theta)^2 + 1 + 2\hat{l}}\right)}. \tag{B5}$$

Appendix C. Derivation of the dimensionless cooperative number

To determine whether a burst event precedes an overlap event in a pore throat, we define the dimensionless cooperative number N_{coop}. Figure 8 shows two adjacent pore throats consisting of three posts with similar diameter d, pore throat size a, and contact angle θ, which is the most representative for our system. The angle between two neighbouring interfaces $\angle$ABC is denoted ϕ. We denote the angle between the line connecting points D and B, and the line connecting A and B, as η_1. Similarly, we denote the angle between the line connecting points G and B, and the line connecting B and C, as η_2.

Increasing the pressure of the invading fluid advances the two adjacent interfaces within the pore throat until they meet (i.e. an overlap event occurs). These two interfaces must satisfy the geometric condition $\eta_1 + \eta_2 = \phi$ (Holtzman & Segre 2015). To determine whether a burst event is preceded by an overlap event, we must calculate η_1 and η_2, corresponding to a burst event, and then calculate λ:

$$\lambda = \phi - (\eta_1 + \eta_2). \tag{C1}$$

Here, $\lambda > 0$ indicates that $\eta_1 + \eta_2 < \phi$, thus a burst occurs before the interfaces can overlap. In contrast, $\lambda < 0$ suggests that $\eta_1 + \eta_2 > \phi$, which means that an overlap event

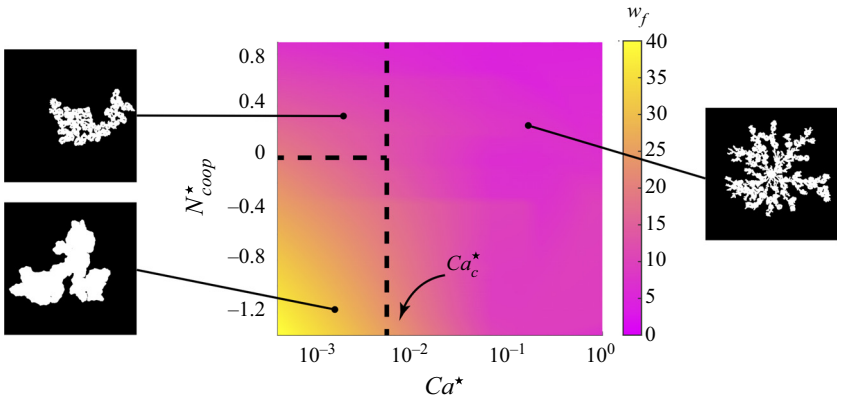

Figure 9. Here, $Ca^{\star}$ and $N^{\star}_{coop}$ explain the variations in w_f in 15 different mixed-wet domains (θ_w–$\theta_o = 30°$–$120°$, $60°$–$120°$, $60°$–$150°$; $f_w = 2\,\%, 26\,\%, 50\,\%, 76\,\%, 98\,\%$) over a wide range of capillary numbers.

will take place and the interfaces merge and form a new fluid–fluid interface. Given that the pore throats in the system are similar, and consequently so are the burst radii of the interfaces, we can rewrite the equation with $\eta_1 = \eta_2 = \eta$ and define the cooperative number N_{coop} as

$$N_{coop} = \frac{\lambda}{2} = \frac{\phi}{2} - \eta. \tag{C2}$$

In figure 8, we connect points P and B to form a line with length d_1. We then define the right triangle BPF with acute angle α given by

$$\alpha = \arccos\left(\frac{a+d}{2d_1}\right). \tag{C3}$$

Applying the cosine law in the triangle BPD gives

$$\frac{d}{2} = \sqrt{r_p^2 + d_1^2 - 2d_1 r_p \cos\beta}, \tag{C4}$$

where $\beta = \pi - \eta - \alpha - \theta$. We rearrange (C4) as

$$\eta = \pi - \arccos\left(\frac{r_p^2 + d_1^2 - \dfrac{d^2}{4}}{2d_1 r_p}\right) - \arccos\frac{a+d}{2d_1} - \theta. \tag{C5}$$

Substituting (C5) into (C2) gives

$$N_{coop} = \frac{\phi}{2} + \theta + \arccos\left(\frac{r_p^2 + d_1^2 - \dfrac{d^2}{4}}{2d_1 r_p}\right) + \arccos\left(\frac{a+d}{2d_1}\right) - \pi. \tag{C6}$$

References

Abdallah, W., *et al.* 1986 Fundamentals of wettability. *Technology* **38** (1125–1144), 268.

Al-Menhali, A.S. & Krevor, S. 2016 Capillary trapping of CO_2 in oil reservoirs: observations in a mixed-wet carbonate rock. *Environ. Sci. Technol.* **50**, 2727–2734.

Al-Menhali, A.S., Menke, H.P., Blunt, M.J. & Krevor, S.C. 2016 Pore scale observations of trapped CO_2 in mixed-wet carbonate rock: applications to storage in oil fields. *Environ. Sci. Technol.* **50**, 10282–10290.

AlRatrout, A., Blunt, M.J. & Bijeljic, B. 2018 Wettability in complex porous materials, the mixed-wet state, and its relationship to surface roughness. *Proc. Natl Acad. Sci. USA* **115**, 8901–8906.

Andrew, M., Bijeljic, B. & Blunt, M. 2014 Pore-scale contact angle measurements at reservoir conditions using X-ray microtomography. *Adv. Water Resour.* **68**, 24–31.

Armstrong, R.T., Sun, C., Mostaghimi, P., Berg, S., Rücker, M., Luckham, P., Georgiadis, A. & McClure, J.E. 2021 Multiscale characterization of wettability in porous media. *Transp. Porous Media* **140** (1), 215–240.

Armstrong, R.T. & Wildenschild, D. 2012 Microbial enhanced oil recovery in fractional-wet systems: a pore-scale investigation. *Transp. Porous Media* **92**, 819–835.

Bachu, S. 2008 CO_2 storage in geological media: role, means, status and barriers to deployment. *Prog. Energy Combust. Sci.* **34**, 254–273.

Bakhshian, S. & Hosseini, S.A. 2019 Pore-scale analysis of supercritical CO_2-brine immiscible displacement under fractional-wettability conditions. *Adv. Water Resour.* **126**, 96–107.

Blunt, M.J. 2001 Flow in porous media – pore-network models and multiphase flow. *Curr. Opin. Colloid Interface Sci.* **6**, 197–207.

Blunt, M.J., Lin, Q., Akai, T. & Bijeljic, B. 2019 A thermodynamically consistent characterization of wettability in porous media using high-resolution imaging. *J. Colloid Interface Sci.* **552**, 59–65.

Bultreys, T., Van Hoorebeke, L. & Cnudde, V. 2016 Simulating secondary waterflooding in heterogeneous rocks with variable wettability using an image-based, multiscale pore network model. *Water Resour. Res.* **52** (9), 6833–6850.

Chang, C., Kneafsey, T.J., Wan, J., Tokunaga, T.K. & Nakagawa, S. 2020 Impacts of mixed-wettability on brine drainage and supercritical CO_2 storage efficiency in a 2.5-D heterogeneous micromodel. *Water Resour. Res.* **56** (7), e2019WR026789.

Cieplak, M. & Robbins, M.O. 1988 Dynamical transition in quasistatic fluid invasion in porous media. *Phys. Rev. Lett.* **60**, 2042–2045.

Cieplak, M. & Robbins, M.O. 1990 Influence of contact angle on quasistatic fluid invasion of porous media. *Phys. Rev.* B **41** (16), 11508–11521.

Cueto-Felgueroso, L. & Juanes, R. 2008 Nonlocal interface dynamics and pattern formation in gravity-driven unsaturated flow through porous media. *Phys. Rev. Lett.* **101**, 244504.

Geistlinger, H., Zulfiqar, B., Schlueter, S. & Amro, M. 2021 New structural percolation transition in fractional wet 3D-porous media: a comparative μCT study. *Water Resour. Res.* **57**, e2021WR030037.

Glass, R.J., Parlange, J.-Y. & Steenhuis, T.S. 1989 Wetting front instability: 1. Theoretical discussion and dimensional analysis. *Water Resour. Res.* **25** (6), 1187–1194.

Guo, R., Dalton, L.E., Fan, M., McClure, J., Zeng, L., Crandall, D. & Chen, C. 2020 The role of the spatial heterogeneity and correlation length of surface wettability on two-phase flow in a CO_2–water–rock system. *Adv. Water Resour.* **146**, 103763.

Haines, W.B. 1930 Studies in the physical properties of soil. V. The hysteresis effect in capillary properties, and the modes of moisture distribution associated therewith. *J. Agric. Sci.* **20**, 97–116.

Herring, A.L., Sun, C., Armstrong, R.T. & Saadatfar, M. 2023 Insights into wettability alteration during cyclic $scCO_2$-brine injections in a layered Bentheimer sandstone. *Intl J. Greenh. Gas Control* **122**, 103803.

Hiller, T., Ardevol-Murison, J., Muggeridge, A., Schröter, M. & Brinkmann, M. 2019 The impact of wetting-heterogeneity distribution on capillary pressure and macroscopic measures of wettability. *SPE J.* **24** (1), 200–214.

Høiland, L.K., Spildo, K. & Skauge, A. 2007 Fluid flow properties for different classes of intermediate wettability as studied by network modelling. *Transp. Porous Media* **70** (1), 127–146.

Holtzman, R. 2016 Effects of pore-scale disorder on fluid displacement in partially-wettable porous media. *Sci. Rep.* **6** (1), 1–10.

Holtzman, R. & Juanes, R. 2010 Crossover from fingering to fracturing in deformable disordered media. *Phys. Rev.* E **82**, 046305.

Holtzman, R. & Segre, E. 2015 Wettability stabilizes fluid invasion into porous media via nonlocal, cooperative pore filling. *Phys. Rev. Lett.* **115**, 164501.

IRANNEZHAD, A., PRIMKULOV, B.K., JUANES, R. & ZHAO, B. 2023 Fluid–fluid displacement in mixed-wet porous media. *Phys. Rev. Fluids* **8** (1), L012301.

KENKEL, N. & WALKER, D. 1996 Fractals in the biological sciences. *Coenoses*, 77–100.

KOVSCEK, A.R., WONG, H. & RADKE, C.J. 1993 A pore-level scenario for the development of mixed wettability in oil reservoirs. *AIChE J.* **39**, 1072–1085.

LAKE, L.W. 1989 *Enhanced Oil Recovery*. Prentice-Hall.

LAN, T., HU, R., YANG, Z., WU, D.-S. & CHEN, Y.-F. 2020 Transitions of fluid invasion patterns in porous media. *Geophys. Res. Lett.* **47** (20), e2020GL089682.

LEE, C., ZHAO, B., ABOUATALLAH, R., WANG, R. & BAZYLAK, A. 2019 Compressible-gas invasion into liquid-saturated porous media: application to polymer-electrolyte-membrane electrolyzers. *Phys. Rev. Appl.* **11**, 054029.

LENORMAND, R., TOUBOUL, E. & ZARCONE, C. 1988 Numerical models and experiments on immiscible displacements in porous media. *J. Fluid Mech.* **189**, 165–187.

LIN, Q., BIJELJIC, B., BERG, S., PINI, R., BLUNT, M.J. & KREVOR, S. 2019 Minimal surfaces in porous media: Pore-scale imaging of multiphase flow in an altered-wettability Bentheimer sandstone. *Phys. Rev.* E **99**, 063105.

MACMINN, C.W., SZULCZEWSKI, M.L. & JUANES, R. 2010 CO_2 migration in saline aquifers. Part 1. Capillary trapping under slope and groundwater flow. *J. Fluid Mech.* **662**, 329–351.

MÅLØY, K.J., FURUBERG, L., FEDER, J. & JØSSANG, T. 1992 Dynamics of slow drainage in porous media. *Phys. Rev. Lett.* **68** (14), 2161.

MOEBIUS, F. & OR, D. 2012 Interfacial jumps and pressure bursts during fluid displacement in interacting irregular capillaries. *J. Colloid Interface Sci.* **377**, 406–415.

MURISON, J., SEMIN, B., BARET, J.C., HERMINGHAUS, S., SCHRÖTER, M. & BRINKMANN, M. 2014 Wetting heterogeneities in porous media control flow dissipation. *Phys. Rev. Appl.* **2**, 034002.

O'CARROLL, D.M., ABRIOLA, L.M., POLITYKA, C.A., BRADFORD, S.A. & DEMOND, A.H. 2005 Prediction of two-phase capillary pressure–saturation relationships in fractional wettability systems. *J. Contam. Hydrol.* **77** (4), 247–270.

ORR, F. & TABER, J. 1984 Use of carbon dioxide in enhanced oil recovery. *Science* **224**, 563–569.

PRIMKULOV, B.K., PAHLAVAN, A.A., FU, X., ZHAO, B., MACMINN, C.W. & JUANES, R. 2019 Signatures of fluid–fluid displacement in porous media: wettability, patterns and pressures. *J. Fluid Mech.* **875**, R4.

PRIMKULOV, B.K., PAHLAVAN, A.A., FU, X., ZHAO, B., MACMINN, C.W. & JUANES, R. 2021 Wettability and Lenormand's diagram. *J. Fluid Mech.* **923**, A34.

PRIMKULOV, B.K., TALMAN, S., KHALEGHI, K., SHOKRI, A.R., CHALATURNYK, R., ZHAO, B., MACMINN, C.W. & JUANES, R. 2018 Quasistatic fluid–fluid displacement in porous media: invasion-percolation through a wetting transition. *Phys. Rev. Fluids* **3**, 104001.

SALATHIEL, R. 1973 Oil recovery by surface film drainage in mixed-wettability rocks. *J. Pet. Technol.* **25** (10), 1216–1224.

SCANZIANI, A., LIN, Q., ALHOSANI, A., BLUNT, M.J. & BIJELJIC, B. 2020 Dynamics of displacement in mixed-wet porous media. *Proc. R. Soc. Lond.* A **476** (2240), 20200040.

SCHROEDER, M.R. 2009 *Fractals, Chaos, Power Laws: Minutes from an Infinite Paradise*, Dover edn. W.H. Freeman and Company.

SINGHAL, A.K., MUKHERJEE, D.P. & SOMERTON, W.H. 1976 Effect of heterogeneous wettability on flow of fluids through porous media. *J. Can. Pet. Technol.* **15** (03), doi:10.2118/76-03-08.

SKAUGE, A. & OTTESEN, B. 2002 A summary of experimentally derived relative permeability and residual saturation on North Sea reservoir cores. In *Paper SCA 2002-12 Presented at the International Symposium of the Society of Core Analysts*, vol. 22, p. 25.

STOKES, J.P., WEITZ, D.A., GOLLUB, J.P., DOUGHERTY, A., ROBBINS, M.O., CHAIKIN, P.M. & LINDSAY, H.M. 1986 Interfacial stability of immiscible displacement in a porous medium. *Phys. Rev. Lett.* **57**, 1718–1721.

SYGOUNI, V., TSAKIROGLOU, C.D. & PAYATAKES, A.C. 2006 Capillary pressure spectrometry: toward a new method for the measurement of the fractional wettability of porous media. *Phys. Fluids* **18** (5), 053302.

SZULCZEWSKI, M.L., MACMINN, C.W., HERZOG, H.J. & JUANES, R. 2012 Lifetime of carbon capture and storage as a climate-change mitigation technology. *Proc. Natl Acad. Sci. USA* **109** (14), 5185–5189.

TOUSSAINT, R., LØVOLL, G., MÉHEUST, Y., MÅLØY, K.J. & SCHMITTBUHL, J. 2005 Influence of pore-scale disorder on viscous fingering during drainage. *EPL (Europhys. Lett.)* **71** (4), 583.

TWEHEYO, M.T., HOLT, T. & TORSÆTER, O. 1999 An experimental study of the relationship between wettability and oil production characteristics. *J. Pet. Sci. Engng*, 179–188.

USTOHAL, P., STAUFFER, F. & DRACOS, T. 1998 Measurement and modeling of hydraulic characteristics of unsaturated porous media with mixed wettability. *J. Contam. Hydrol.* **33**, 5–37.

WARNER, N.R., JACKSON, R.B., DARRAH, T.H., OSBORN, S.G., DOWN, A., ZHAO, K., WHITE, A. & VENGOSH, A. 2012 Geochemical evidence for possible natural migration of Marcellus Formation brine to shallow aquifers in Pennsylvania. *Proc. Natl Acad. Sci. USA* **109** (30), 11961–11966.

YANG, J., SAADAT, M., AZIZOV, I., DUDEK, M., ØYE, G. & TSAI, P.A. 2022 Wettability effect on oil recovery using rock-structured microfluidics. *Lab Chip* **22**, 4974.

ZHAO, B., LEE, C.H., LEE, J.K., FAHY, K.F., LAMANNA, J.M., BALTIC, E., JACOBSON, D.L., HUSSEY, D.S. & BAZYLAK, A. 2021 Superhydrophilic porous transport layer enhances efficiency of polymer electrolyte membrane electrolyzers. *Cell Rep. Phys. Sci.* **2** (10), 100580.

ZHAO, B., MACMINN, C.W. & JUANES, R. 2016 Wettability control on multiphase flow in patterned microfluidics. *Proc. Natl Acad. Sci. USA* **113** (37), 10251–10256.

ZHAO, B., *et al.* 2019 Comprehensive comparison of pore-scale models for multiphase flow in porous media. *Proc. Natl Acad. Sci. USA* **116** (28), 13799–13806.